Journal of Institute of Science and Technology, 31(1), 45-64 (2026)
ISSN: 2467-9062 (print), e-ISSN: 2467-9240
https://doi.org/10.3126/jist.v31i1.86526

Research Article

DFT STUDY OF ELECTRONIC PROPERTIES, SPECTROSCOPIC ANALYSIS, AND THERMODYNAMIC PARAMETERS OF CLEOMIN

Dipak Thapa[1§], Krishna Bahadur Rai[1,2,*§], Tulsi Ojha[1], Madhav Prasad Ghimire[2*]

[1]*Department of Physics, Patan Multiple Campus, Lalitpur, Tribhuvan University, Nepal*
[2]*Central Department of Physics, Tribhuvan University, Nepal*
[*]*Correspondence: krishna.rai@pmc.tu.edu.np; madhav.ghimire@cdp.tu.edu.np*
[§]*These authors contributed equally*

(***Received:*** *February 18, 2026;* ***Revised:*** *March 30, 2026;* ***Accepted:*** *May 12, 2026)*

ABSTRACT

Cleomin, a saturated heterocyclic and nonlinear organic molecule of pharmacological importance, yet it's structural, electronic, and thermodynamic properties have not been adequately characterized at the molecular level. In this study, density functional theory calculations were performed at the B3LYP/6-311++G(d,p), WX97XD/6-311++G(d,p), and WX97XD/6-31++G(d,p) levels of theory, supplemented by a potential energy surface scan to understand the conformational stability of the Cleomin, whereas B3LYP/6-311++G(d,p) basis set was employed to examine the electronic behavior and thermodynamic properties of Cleomin. The optimized geometry of the Cleomin revealed a stable configuration with no imaginary frequencies. Non-covalent interaction - Reduced density gradient analysis identified dominant van der Waals interactions alongside weak hydrogen-bonding and steric repulsion within the ring system. The electron localization function and localized orbital locator maps showed a strong electron localization of electrons at hydrogen and sulphur atoms and the spatial distribution of bonding regions and lone pairs. The molecular electrostatic potential mapping showed electronegative regions around S1 and O2 as electrophilic attack sites and electropositive regions near nitrogen-bonded hydrogen as nucleophilic attack sites. Frontier molecular orbital analysis yielded an energy gap of 5.23 eV, confirmed by the density of states spectrum, indicating chemical stability and low reactivity. Mulliken charge analysis identified S1 and H17 as the primary reactive centers. Natural bonding orbital analysis revealed strong hyper-conjugative interaction from N3[LP(1)] to S1-C9($\sigma*$) with a stabilization energy of 68.90 kcal/mol, and Fukui function analysis clearly distinguished sites for nucleophilic and electrophilic attack. Vibrational wavenumbers showed excellent agreement with reported FT-IR data, and thermodynamic parameters (i.e., Specific heat capacity, Entropy and Enthalpy) increased consistently with rising temperature. These findings offer a valuable foundation for the potential applications of Cleomin in drug design and medicinal chemistry.

Keywords: Cleomin, Density functional theory, Electronic structure, Thermodynamical parameters, Vibrational analysis

INTRODUCTION

Cleomin ($C_6H_{11}NOS$) is a 1,3-oxazolidine-2-thione compound, first defined in 1963. The structure is non-linear heterocyclic due to the attached substituent groups, hybridization, and the functional group attached in the ring. Cleomin is produced as the end product of the enzymatic hydrolysis of glucocleomin (Kjaer, 1963). The compound has been extracted from the roots of Ritchiea longipediellata, with its identification confirmed through chromatography of the methanolic extract and various spectroscopic techniques (Oguakwa et al., 1981). More recently, it has also been reported from the roots of Capparaceae Neocalyptrocalix longifolium (Opretzka et al., 2023). Furthermore, Catabolites of isoleucine may serve as precursors of Cleomin biosynthesis (Oguakwa et al., 1981). Cleomin, with a single chiral center of 4, contains one sp^2 hybridized carbon and one sp^3 hybridized C. Due to its potentiality of chemistry and bioactivity for Cleomin, bio-engineering could be used in medical science, agriculture, organic chemistry (Oguakwa et al., 1981; Opretzka et al., 2023). Its interactions with enzymes, receptors and other biological systems lead to the possibility to have a range of therapeutic properties, such as its favorable effects on heart diseases and anticancer activity (Oguakwa et al., 1981; Opretzka et al., 2023). Besides this, it's potential as plant growth-regulator and bio-pesticide

accounts for the importance of this compound to sustainable approach in agriculture (Kjaer, 1963).

Over the past few years, heterocyclic compounds structurally related to oxazolidine-2-thiones have also been extensively studied theoretically. Using Density Functional Theory (DFT) with the B3LYP functional and the 6-31G(d) basis set, for example, vibrational spectra and molecular electrostatic potential of 5-(3-pyridyl methylidene)-thiazolidine-2-thione-4-one have been performed (Pirnau et al., 2008). Likewise, theoretical studies on 1,3-thiazolidine-2-thione and 1,3-oxazolidine-2-thione derivatives indicated that the thiocarbonyl group has a partial positive charge and the oxygen atom possesses negative charge that these systems can exist in keta-contract forms with appreciable delocalization of S=C–N fragment (Roux et al., 2009). More recently, furanose-fused oxazolidine-2-thiones have been explored on this account given their nucleophilic sulfur and nitrogen centers that promote both S-arylation and N-arylation in functionalization strategies of copper catalysis (Kederiene et al., 2022). These results highlight the impact of computational methods in understanding structural, electronic and thermodynamic aspects of oxazolidine-2-thione-based compounds. Even though increasing attention on the study of heterocyclic compounds, no extensive theoretical study for Cleomin molecule has yet reported. In particular, a detailed investigation of its optimized molecular geometry, electronic structure, non-covalent interactions, vibrational behavior and thermodynamic properties using high-level Density Functional Theory with basis set 6-311++G (d, p) has not been performed using DFT analysis. The lack of such theoretical information represents a considerable gap in research regarding the biological and chemical importance of the molecule. Thus, a thorough computational study is required to assess the electronic distribution-properties, molecular stability and thermodynamic characteristics of Cleomin in a quantum-chemical approach.

A thorough DFT study of the Cleomin molecule is presented in the current work. Results encompass optimized molecular geometry, non-covalent interaction (NCI) analysis by the reduced density gradient (RDG), electron localization function (ELF), localized orbital locator (LOL), molecular electrostatic potential (MEP) and electrostatic potential (ESP) surfaces, electron density (ED) distribution, highest occupied molecular orbital (HOMO), lowest unoccupied molecular orbital(LUMO), density of states (DOS), global reactivity parameters, mulliken atomic charges, natural bonding orbital (NBO) analysis, Fukui function analysis, vibration characteristics as well as thermodynamic properties. Overall, the findings of this study will offer better insights into the structural stability, electronic properties and thermodynamic behavior of Cleomin while paving the way for future experimental and theoretical studies on biologically relevant oxazolidine-2-thione analogues.

MATERIALS AND METHODS

Computational methodology and theoretical details

The computations of Cleomin were executed using Gaussian 09W software (Frisch et al., 2009) by means of the DFT/B3LYP technique using 6-311++G(d,p), WX97XD/6-311++G(d,p), and WX97XD/6-31++G(d,p) levels basis set for molecular optimization. Furthermore, we used the B3LYP function for the rest of the calculations and results because it has been tested and proven to work effectively. We are focusing on the B3LYP function and the molecule structure. The optimized molecular structures of Cleomin were visualized using GaussView 6.0 software (Dennington et al., 2009). The modes of vibrations were characterized using the optimized structural parameters in along with HOMO-LUMO, MEP, ESP, and ED. The DOS spectrum was observed with the help of the GaussSum 3.0 program (O'Boyle et al., 2008). Multiwfn and Visual Molecular Dynamics (VMD) software were used to obtain iso-surface maps of NCI, RDG, ELF, and LOL (William, 1996). The thermodynamic parameters were obtained from the Moltran Program (Ignatov, 2004).

The reactivity parameters such as Electron affinity (A), Ionization potential (I), Electronegativity (χ), Chemical hardness (η), Chemical potential (μ), electronic pliability (S), Electrophilic reactivity (ω) were calculated from HOMO-LUMO energies by the use of Koopmans' theorem (Chand et al., 2015; Bisong et al., 2020), such that:

$$I = -E_{HOMO} \quad (1)$$

$$A = -E_{LUMO} \quad (2)$$

Where I and A are the ionization potential and electron acceptance ability of an atom, respectively.

Similarly, the electronegativity index (χ) of the molecule is

$$\chi = \frac{I+A}{2} \quad (3)$$

The hardness (η) is defined as

$$\eta = \frac{I-A}{2} \quad (4)$$

The chemical potential (μ) is

$$\mu = \frac{I+A}{2} \quad (5)$$

The chemical softness is the reciprocal of the chemical hardness

$$S = \frac{1}{\eta} \quad (6)$$

The Electrophilicity index (ω) is obtained as

$$\omega = \frac{\mu^2}{2\eta} \quad (7)$$

Likewise, the interaction-related NCI-RDG plots were generated using VMD version 1.9.4a53 (William, 1996). The RDG analysis was carried out based on the following mathematical expression of RDG for the molecule (Johnson et al., 2010),

$$RDG(r) = \frac{\left|\frac{\nabla\rho(r)}{\rho(r)}\right|^{\frac{4}{3}}}{2(3\pi^2)^{\frac{1}{3}}} \quad (8)$$

In this equation, ∇ρ(r) indicates how the electron density ρ(r) changes at a specific point in the molecule.

The topological analysis, including ELF and LOL, was carried out using Multiwfn version 3.8 (Lu & Chen, 2012). The ELF is described by the following equation (Becke & Edgecombe, 1990),

$$ELF = \frac{1}{1+\left(\frac{D}{D_h}\right)^2} \quad (9)$$

With $D = \frac{1}{2\sum_i|\varphi_i(r)|^2} - \frac{1}{8\left[\frac{|\nabla\rho|^2}{\rho}\right]}$ and $(D_h) = \frac{3(3\pi^2)^{\frac{2}{3}}\rho^{\frac{5}{3}}}{10}$.

Here, D stands for the redundancy kinetic energy, while D_h represents its corresponding reference value.

The LOL analysis was conducted using the Schmider and Becke formulation (Schmider & Becke, 2002),

$$LOL(r) = \frac{\tau(r)}{1+\tau(r)} \quad (10)$$

Where τ(r) represents a dimensionless variable and

$$\tau(r) = \frac{g_0(r)}{g(r)} = \frac{2D_0(r)}{\sum_i\eta_i|\nabla\varphi_i(r)|^2} \quad (11)$$

Here, g(r) denotes the electron kinetic energy, φ_i refers to the Hartree-Fock orbitals, and $D_0(r)$ represents the value for a spin-polarized system.

RESULTS AND DISCUSSION

Structural optimization

Figure 1 shows the geometry-optimized molecular structure of Cleomin along with atomic labels and symbols using B3LYP/6-311++G(d,p), WX97XD/6-311++G(d,p), and WX97XD/6-31++G(d,p) levels via DFT. The minimum stable energy, dipole moment, point group, and predicted energy change of a molecule in each level are tabulated in Table 1. As observed from Table 1, the optimized total energies of the $C_6H_{11}NOS$ molecule are -20778.01 eV, -20773.64 eV, and -20771.00 eV respectively, indicating a stable equilibrium geometry with respective dipole moments. In the optimized structure, C4 is identified as chiral (S) carbon atom, C9 is a sp^2 hybridized atom, and C4, C5, C6, C7, and C8 are sp^3 hybridized atoms. All optimized structures were verified to be true local minima on the potential energy surface (PES) by confirming the absence of imaginary vibrational frequencies in the subsequent frequency calculations

Table 1. Optimized energy(eV), Dipole moment (Debye), Point group in B3YLP/6-311++G(d,p), WX97XD/6-311++G(d,p), WX97XD/6-31++G(d,p) levels of Cleomin using DFT

Methods	Basis set	Energy	Dipole moment	Point group
B3LYP	6-311++G(d,p)	-20778.01 eV	6.57 Debye	C_1
WB97XD	6-311++G(d,p)	-20773.64 eV	6.52 Debye	C_1
WB97XD	6-31++G(d,p)	-20771.00 eV	6.58 Debye	C_1

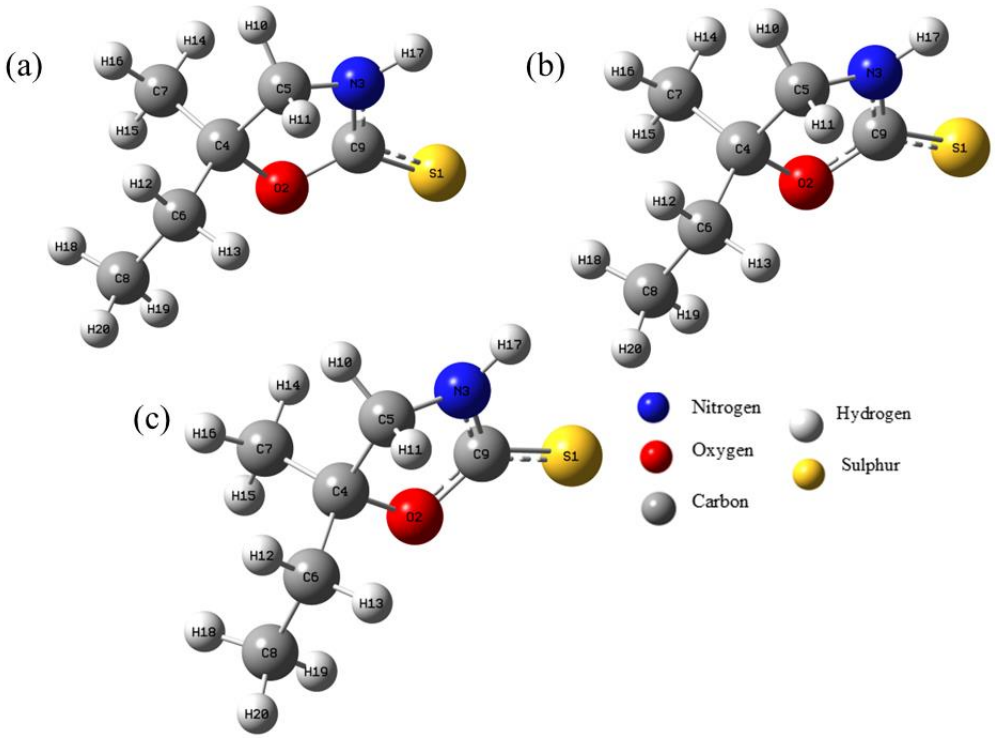

Figure 1. Geometry-optimized molecular structure of Cleomin via DFT using: (a) B3LYP/6-311++G(d,p) (b) WX97XD/6-311++G(d,p) (c) WX97XD/6-31++G(d,p) levels

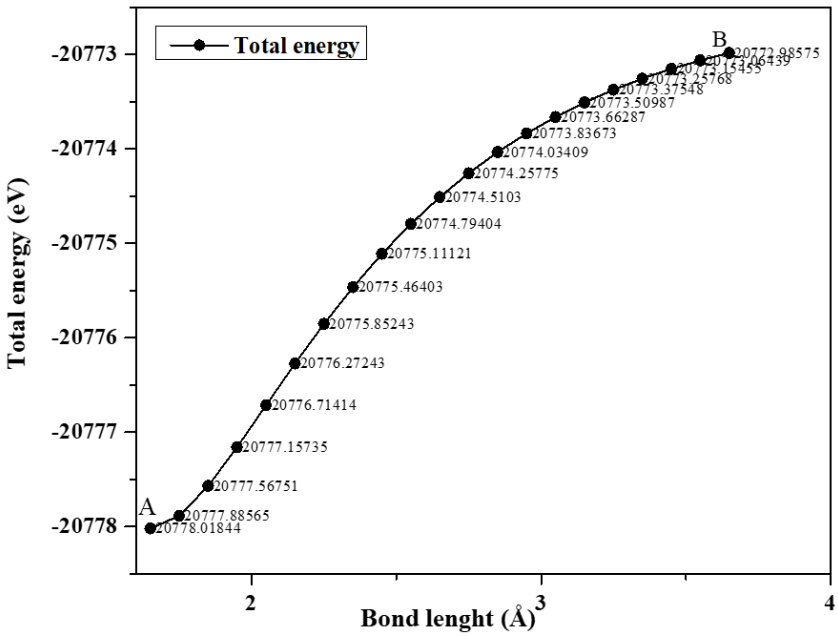

Figure 2. Potential energy surface scan of Cleomin at bond length (S1-C9) in a gaseous state using B3LYP/6-311++G(d,p) basis sets

Figure 2 represents the molecule's lowest energy configuration (minima) in the given constraints and is obtained by scanning the relaxed co-ordinate of bond length between atoms S1 and C9 taking 21 steps with the bond length of 0.1 Å. The molecule achieved its most stable optimized geometry at its lowest point (A) in the curve with energy -20778.01 eV.

Bond distance, bond angle, and torsion angle

Table 2 and Table 3 show the bond distances and bond angles between the atoms of Cleomin. We observed that the bond distance of the molecule lies between 1.00 Å and 1.65 Å. It is found that the average bond length between C-C, C-H, C-N, and C-O is 1.53 Å, 1.09 Å, 1.35 Å, and 1.34 Å, respectively, which are in agreement with the standard C-C, C-H, C-N, and C-O bond lengths (Ram et al., 2019). The bond length between C9-S1 is 1.65 Å and is the highest value, suggesting a relatively weaker bond in comparison to other bonds within the molecule. The bond length between N3-H17 is 1.00 Å, indicating the strongest bond among bonds present within the molecule. The highest bond angle and torsion angle values for S1-C9-N3 and S1-C9-O2-C4 are 127.46° and 175.11°, respectively. This shows that S1-C9-N3 and S1-C4-O2-C4 are less stable in comparison to other bond angles.

Table 2. Bond distance and its values (Å) of Cleomin

Bond distance	Values (Å)	Bond distance	Values(Å)
C9-S1	1.65	C6-H13	1.09
C9-O2	1.34	C6-H12	1.09
C9-N3	1.35	C6-C8	1.53
C9-O2	1.47	C8-H20	1.09
C4-C5	1.54	C8-H18	1.09
C4-C6	1.53	C8-H19	1.09
C4-C7	1.52	C8-H10	1.09
C7-H14	1.09	C5-H11	1.09
C7-H16	1.09	C5-N3	1.45
C7-H15	1.09	N3-H17	1.00
C6-H13	1.09		

Table 3. Bond angle and Torsion angle of Cleomin

Bond angle	Values (°)	Torsion angle	Values (°)
O2-C9-S1	123.89	S1-C9-N3-H17	10.78
S1-C9-N3	127.46	S1-C9-O2-C4	175.11
O2-C9-N3	108.63	C9-N3-C5-H11	-98.77
C9-N3-H17	119.38	C9-N3-C5-H10	139.18
C9-N3-C5	112.44	H17-N3-C5-H11	58.85
H17-N3-C5	124.32	H17-N3-C5-H10	-63.17
N3-C5-H11	111.70	N3-C5-C4-C6	93.27
N3-C5-H10	111.70	H17-N3-C9-O2	-169.48
H10-C5-H11	108.72	C9-O2-C4-C6	-102.19
N3-C5-C4	100.77	C9-O2-C4-C7	135.99
C5-C4-O2	102.44	H11-C5-C4-O2	98.22
C5-C4-C7	113.41	H10-C5-C4-O2	-139.45
C5-C4-C6	112.87	C9-O2-C4-C5	16.40
O2-C4-C7	107.12	O2-C4-C7-H14	66.02
O2-C4-C6	106.19	O2-C4-C7-H15	-53.86
C4-C7-H16	110.67	O2-C4-C7-H16	-173.78
C4-C7-H14	110.58	O2-C4-C6-H13	61.06
C4-C7-H15	110.22	O2-C4-C6-H12	-53.13
H16-C7-H15	108.40		
H15-C7-H14	108.42		

Non-covalent interaction index (NCI) - Reduced density gradient (RDG) analysis

A reduced density gradient helps identify areas of non-covalent interaction including hydrogen bonding, Van der Waals, and electrostatic interaction. High reduced density gradient values show sharp changes in electron density, characteristics of non-bonded regions, whereas low RDG values indicate the presence of weak non-covalent interactions (Arulaabaranam et al., 2021). Although the existence of non-covalent interaction is determined by reduced density gradient values, the strength and nature of the different types of interactions are further characterized by the descriptor sign$\lambda_2\rho(r)$, such that the term 'sign' is a mathematical symbol (positive or negative) of the second eigenvalue, λ_2 is the second eigenvalue of the Hessian matrix of electron density, and $\rho(r)$ is the electron density at position r (Tahenti et al., 2022).

A positive value of sign$\lambda_2\rho(r)>0$ (i.e., red region) corresponds to repulsive interactions such as steric clashes, a negative value of sign$\lambda_2\rho(r)<0$ (i.e., blue region) indicates attractive interactions such as hydrogen bonding and a value of sign$\lambda_2\rho(r)\approx0$ (i.e., green region) represents weak Van der Waals interactions (Chaudhary et al., 2023). Figure 3a presents the non-covalent interaction iso-surface map of Cleomin, in which prominent red spindle-shaped within the ring and ethyl group signify significant steric repulsion. The green iso-surface on the ethyl (CH_2CH_3) group confirm the presence of weak Van der Waals interactions. The lack of blue iso-surface suggests that no hydrogen bonding is present within the molecule. These non-covalent interactions collectively contribute to the overall conformational stability of Cleomin. Figure 3b displays the RDG scatter plot, showing the correlation between the RDG values and sign$\lambda_2\rho(r)$. The red spikes in the reduced density gradient iso-surface map and scatter graph confirms strong steric repulsion, the green spikes ($\rho(r)\approx0$) indicates the existence of Van der Waals interactions among atoms. Nevertheless, the lack of the blue spikes suggests the absence of hydrogen bonding interactions (Chaudhary et al., 2023).

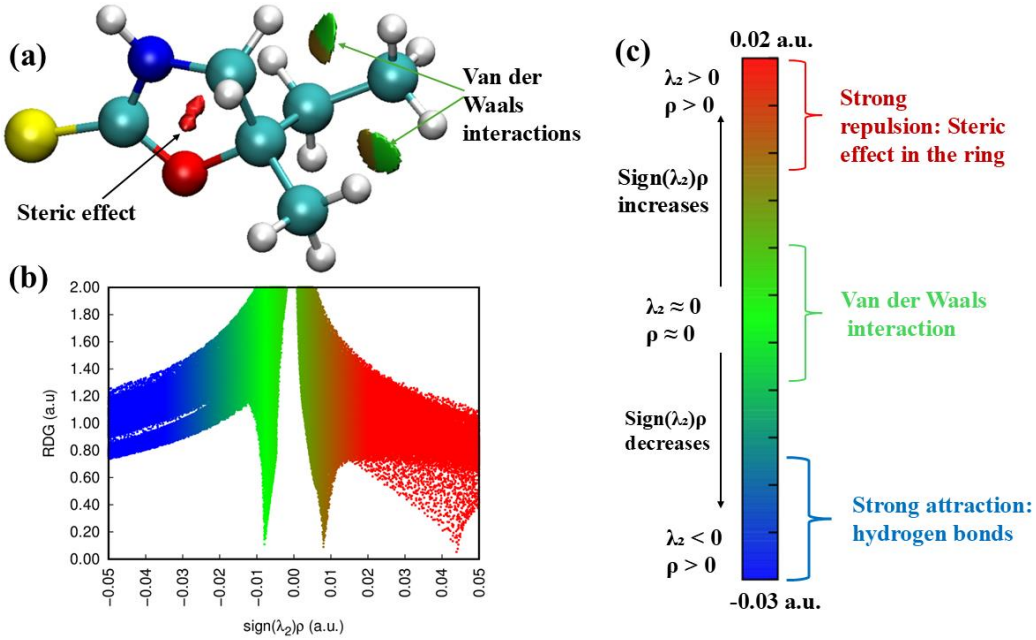

Figure 3. (a) NCI analysis (b) RDG iso-surface map (c) Scatter graph plot of RDG (NCI).

Electron Localization Function (ELF) and Localized Orbital Locator (LOL) analysis

The electron localization function helps to identify bond types and atomic shell structures by measuring the probability of finding an electron near a reference electron of the same spin, while the localized orbital locator shows orbitals overlap and inter-atomic interactions within the molecule (Jacobsen, 2008; Shilpa et al., 2023). High electron localization function and localized orbital locator values indicate strong electron localization arising from lone pairs, core electrons, or covalent bonds, whereas low values reflect electron delocalization across the molecular framework (Rajalakshmi & Vetrivel, 2020; Shilpa et al., 2023). In both ELF and LOL visual representations, varying color gradients ranging from blue to red represent the degree of electron localization, with red denoting high localization and blue denoting delocalization (Arulaabaranam et al., 2021).

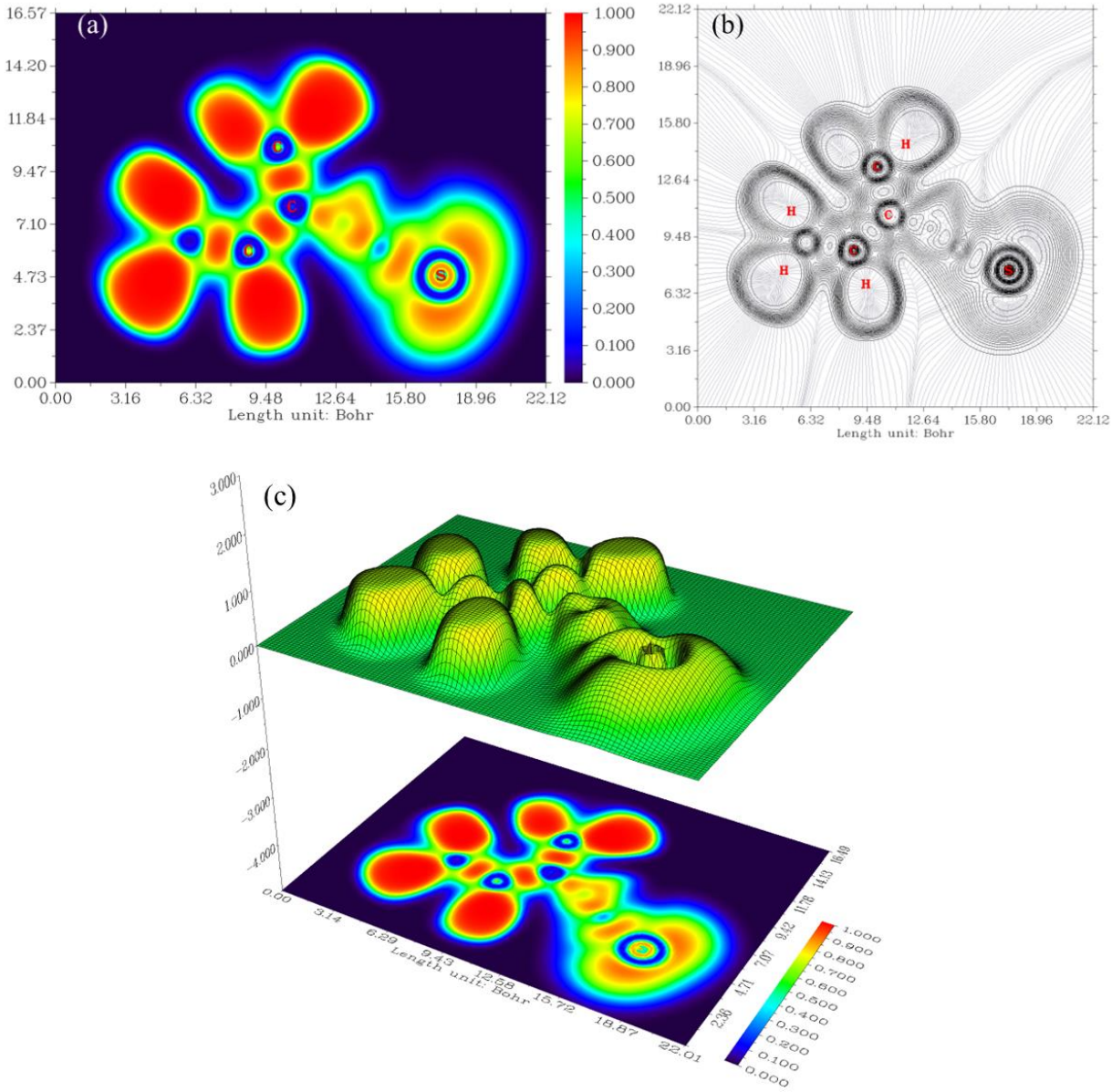

Figure 4. ELF (a) colored filled map, (b) counter map, (c) a projection of a shaded surface map depicting an electronic environment

Figures 4 and 5 show the electron localization function and localized orbital locator of Cleomin, respectively. In Figure 4a, blue rings are surrounding carbon and sulfur atoms (ELF < 0.5) indicate electron delocalization in these regions (Janani et al., 2021). In contrast, red regions with high ELF values (0.5–1.0) concentrated around hydrogen atoms confirm strong electron localization, indicative of covalent bonding character or inner shell electron density (Janani et al., 2021). Figure 4b presents gradient maps with contour lines illustrating the spatial variation of ELF values across the molecular plane. The dense contour shading surrounding H, C, and S atoms reflects regions of high electron density and strong bonding character. Figure 4c displays a 3D ELF surface alongside 2D heat map, where values approaching unity denote strong electron localization and values approaching zero indicate delocalization (Savin et al., 1997). Prominent ELF peaks are observed near Sulphur and hydrogen atoms, reflecting strong electron localization at these centers, whereas carbon atoms exhibit comparatively lower localization. The colour scale follows a blue-to-red gradient, where red regions represent highly localized electrons and blue-to-green regions correspond to delocalized electron density (Savin et al., 1997; Savin, 2005). In Figure 5a, the white space around hydrogen atoms in the localized orbital locator map means very high electron density-higher than 0

(Chaudhary & Joshi, 2022). Red circular regions between carbon atoms further confirm the presence of bonding electron pairs in C-C bonds. Blue regions surrounding carbon and Sulphur atoms denote electron-deficient or delocalized zones. Figure 5b shows that double rings pattern around non-heavy atoms are characteristic of lone pairs or regions of strong electron localization (Dhanalakshmi et al., 2023). The region of high intensity around H, C, O, and S indicates the highly localized nature of core and bonding electrons present in the atom (Becke et al., 1990; Schmider et al., 2000). Notably, the contours lines around sulphur are more widely spaced compared to those around oxygen, indicating relatively greater delocalization of valence electrons on Sulphur. In Figure 5c, each prominent peak corresponds to a region of strong electron localization around Sulphur and hydrogen atoms, consistent with the presence of lone pairs or covalent bonds. The taller peaks associated with hydrogen reflects higher LOL values and stronger localization (Jacobsen, 2008). The chain-like arrangement of peaks within the ring structure mirrors the cyclic bonding framework of Cleomin (Rajalakshmi & Vetrivel, 2020; Ojha et al., 2025). The 2D heat map uses a blue-to-red color bar to show electron localization, with blue for low and red/white for high (Jacobsen, 2008). Red/white circles around hydrogen mark high localized orbital locator values, while yellow-green areas indicate moderate localization. Bright red and white spots show electron localization centers, matching 3D peaks. Blue areas around sulphur and carbon indicate low localization or electron-deficient regions (Rajalakshmi et al., 2020; Jacobsen, 2008).

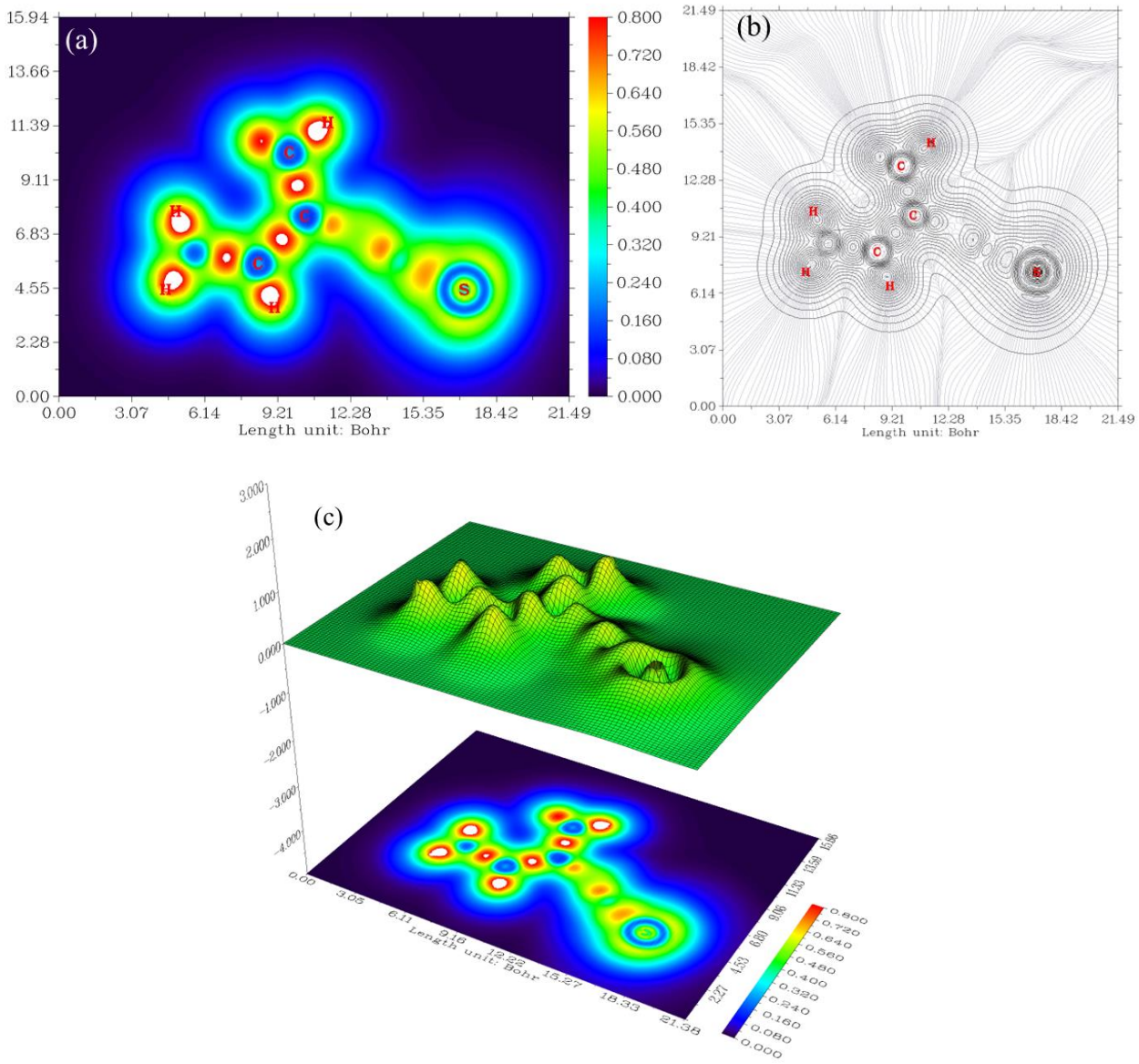

Figure 5. LOL (a) colored filled map, (b) counter map, (c) a projection of a shaded surface map depicting an electronic environment of Cleomin

Molecular Electrostatic Potential (MEP), Electrostatic Potential (ESP), and Electron Density (ED) analysis

Molecular Electrostatic Potential is a graphic representation that shows how electrostatic potential is distributed around a molecule. It sheds insight into the reactivity and interaction locations of the molecule by mapping the regions of distribution of positive and negative charges (Mathammal et al., 2016). Figure 6a represents the transparent view of molecular electrostatic potential, and this molecular electrostatic potential of the molecule ranges between -5.392e-2 a.u. to 5.392e-2 a.u. with a distinct colour gradient. Red and yellow represent electron-rich areas, where the electrostatic potential is negative, and blue represents electron-deficient areas, where the electrostatic potential is positive (Bakheit et al., 2022). In Figure 6a, the red area, a negative electrostatic potential of Cleomin, is mostly seen around S1 and O2 and is readily attributed by lone pairs of electrons (Bakheit et al., 2022), suggesting that S1 and O2 of Cleomin have greater energy levels. Therefore, they are easily subjected to sites for electrophilic attack and can donate electrons as electron donors.

The blue region, denoting a positive electrostatic potential of Cleomin tends to locate mainly around the amino group (N3-H17), indicating the lower energy level and easy availability of sites for nucleophilic attacks, which acts as an acceptor region of the molecule. Figure 6b shows the electrostatic potential on a mesh surface representation of the molecule, indicating charge distribution and reactivity hotspots. The potential ranged from -2.263e-2 a.u. (red, for the electrophilic points) to 2.263e-2 a.u. (blue, for the nucleophilic points). Such a kind of analysis would be helpful in finding out sites for nucleophilic and electrophilic attacks and predicting the level of reactivity and stability, which will be useful to know insights on the molecular behavior and interaction as well as designing reactions (Basnet et al., 2024). In Figure 6b, the red surface near O2 represents negative electrostatic potential due to the high electronegativity of oxygen, which withdraws electron density and generates a region of negativity (Lakshminarayanan et al., 2021) whereas the remaining part of the surface depicts local positive potential, which is representative for this portion of the surface by means of nucleophilic attack. A visualization in a weaker potential (lighter green) is seen, which likely corresponds to the electron density distribution or interactions. When compared to Figure 6a, this one shows a more localized MEP region with a narrower range of molecular electrostatic potential, meaning less polarization or change in electron density (Lakshminarayanan et al., 2021). Figure 6c shows, based on the DFT calculation, a flat charge distribution and the probability of existence of electrons at certain locations.

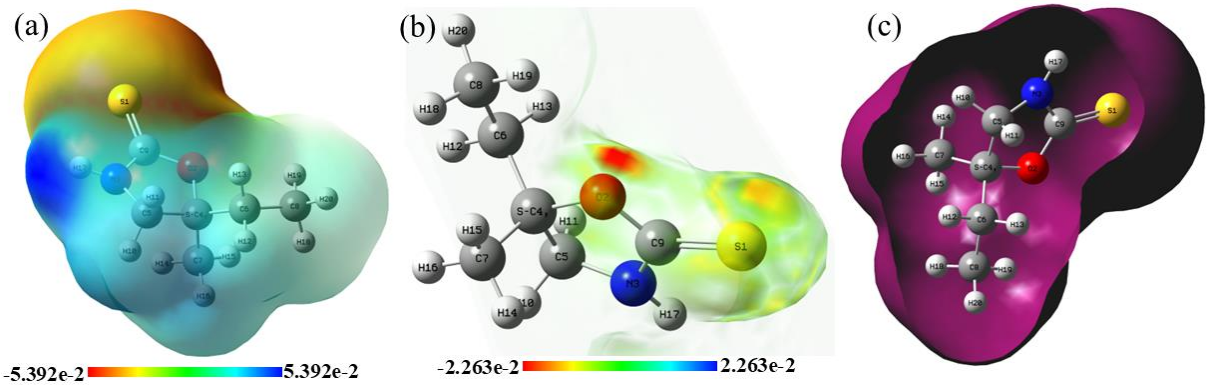

Figure 6. (a) MEP, (b) ESP, and (c) ED of the Cleomin

Frontier Molecular Orbital (FMO)

The HOMO and LUMO are the frontier orbitals determining the molecular reactivity of a compound. HOMO and LUMO are the electron donor region and electron acceptor region, respectively. The frontier molecular orbital sights the knowledge of the properties such as stability, reactivity, transition and optical polarizability, and chemical hardness-softness

of a molecule (Budha & Rai, 2024). A small HOMO-LUMO energy difference indicates a molecule of lower stability and higher reactivity. On the other hand, a high HOMO-LUMO gap (energy difference) means higher stability and less reactivity. The smaller the energy gap, the more intense the electronic transition, and vice versa (Sworakowski, 2018). The HOMO and LUMO plot for $C_6H_{11}NOS$ molecule is illustrated in Figure 7. According to the DFT calculation, the HOMO and LUMO energies of the molecule are -5.88 eV and -0.65 eV respectively (also, negative values indicate a stable nature). A higher energy gap (HOMO-LUMO difference) of 5.23 eV suggests a molecule is hard, having good kinetic stability and relatively low global chemical reactivity. The higher kinetic stability is in fact due to a higher energy gap that increases the energy barrier for electron excitation and chemical reactivity (Miar et al., 2021) or the electronic transition will be difficult (Sworakowski, 2018). However, overall molecular stability also depends on the local structural features, frontier-orbital energies, and environmental factors (i.e., solvation effects, temperature, etc.). Therefore, the HOMO-LUMO energy gap can be taken as one factor among several that contributes to molecular stability (Kumar et al., 2023).

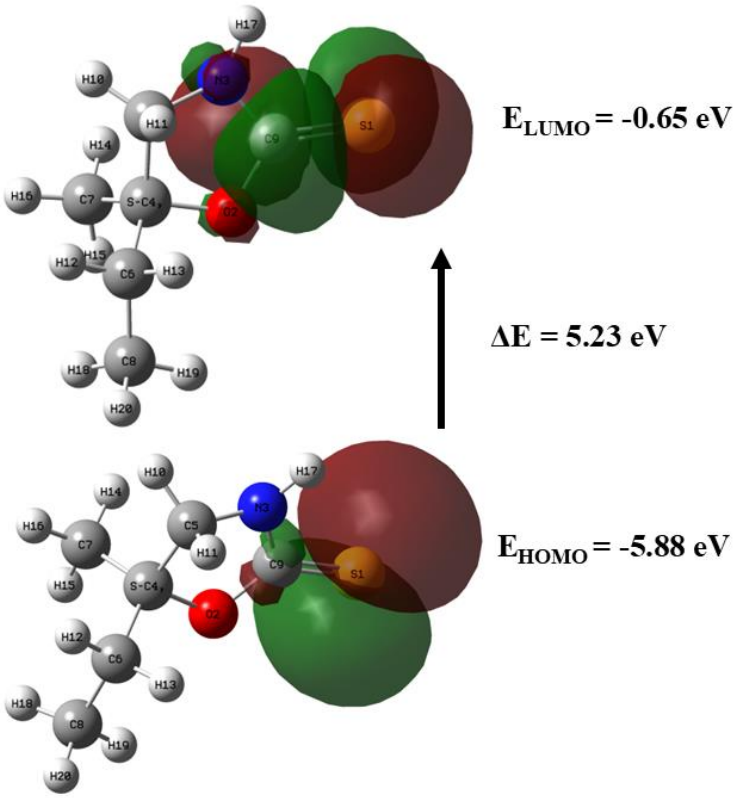

Figure 7. Plot of HOMO-LUMO of the Cleomin

Density of States (DOS)

DOS gathers essential insights and outlines the electronic properties of the molecule. It is utilized to excite electrons from the ground state to the lowest unoccupied energy band, and emphasizing the role of electrons in both the valence and conduction bands (Khalili et al., 2021). DOS helps one to see the creation of energy bands and how they are filled by electrons. DOS spectra (both occupied and virtual orbitals) are shown in Figure 8. The DOS spectrum exhibits an energy gap of 5.19 eV and indicates that electrons require 5.19 eV of energy to move from the highest occupied state to the lowest unoccupied state. The energy gap obtained from the HOMO-LUMO analysis is in good agreement with this energy gap based on the DOS spectrum.

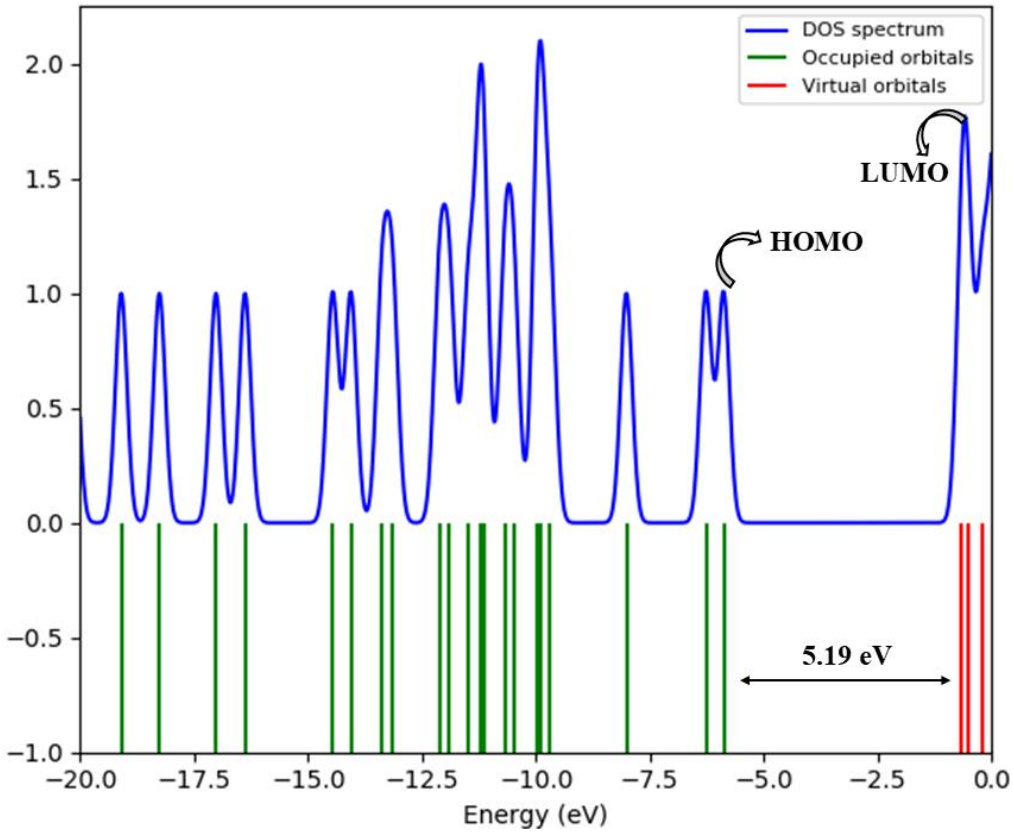

Figure 8. DOS spectrum of the Cleomin molecule.

Global reactivity parameters

The global reactivity descriptors, as defined in the context of DFT, consist of Ionization potential (I), Electron affinity (A), Electronegativity (χ), Chemical hardness (η), Chemical potential (μ), Chemical softness(S) and Electrophilicity index (ω). These parameters describe the stability and reactivity features of the molecule. These are computed from the HOMO-LUMO energy level using Koopman's theorem such that, $I = -E_{HOMO}$ and $A = -E_{LUMO}$ (Chand et al., 2015; Bisong et al., 2020). Ionization energy is the energy of removing an electron from an atom, while electron affinity measures the energy released when an atom gains one electron (Chand et al., 2015). The calculated I and A are 5.88 eV, and 0.65 eV, respectively. The electronegativity, 2.18 eV, analyzed is an indicator of the ability of an atom to attract valence electrons in a chemical compound. The calculated chemical hardness of 2.61 eV shows that the molecule is very stable and not easy to change its electron distribution. The calculated chemical potential of –2.18 eV shows the storage energy as a substance, and the more negative the value, the larger the propensity to release or react to the product. The negative of the total hardness is the chemical softness, which reflects how easily a molecule can gain or lose electrons (Bishwokarma et al., 2025). The derived chemical softness value of 0.38 eV^{-1} can be used to interpret both the polarizability of the molecule, and its electron transfer ability. A measure of the molecule's ability to attract electrons in a chemical reaction is its electrophilicity index, which is 0.91 eV.

Mulliken atomic charge

Mulliken charge calculates how electronic charge is spread throughout a molecule (Uprety et al., 2024). It examines the arrangement of electrons and allocates a charge to each atom according to this distribution. It is determined by the Mulliken Population Analysis method, such that it serves as a complement to the MEP, offering a distribution of the net atomic charges within the molecule (Alrabiah et al., 2017). Figure 9 represents the histogram of Mulliken charge distribution for each atom of the $C_6H_{11}NOS$ molecule, which displays that the hydrogen atoms possess positive charge, however, all the carbon atoms except C4 and C9 possess negative charge. Here, H17 has a higher positive Mulliken charge, and S1 has the most negative Mulliken charge.

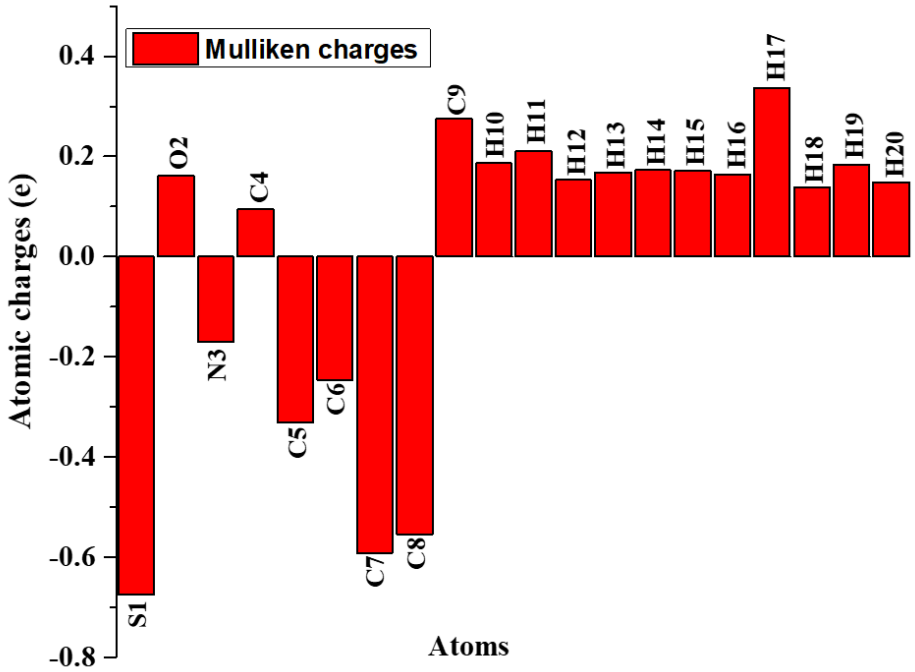

Figure 9. Histogram of Mulliken atomic charge distribution of the Cleomin molecule

Natural Bond Orbital (NBO) analysis

In this study, the second-order Fock matrix was employed within the NBO analysis to quantify donor-acceptor interactions, and the stabilization energy associated with this specific delocalization or hyperconjugation pathway from a donor (i) to an acceptor (j) (Elanthiraiyan et al., 2015) is estimated using the following relationship:

$$E(2) = \Delta E_{ij} = q_i \frac{F(i,j)^2}{E_j - E_i} \qquad (12)$$

Where, E(2) is the stabilization energy, q_i is the donor orbital occupancy, E_j and E_i are the diagonal elements and F(i,j) is the off-diagonal NBO Fock matrix element.

A larger stabilization energy value signifies a more intense electron donor-acceptor interaction, reflecting both a greater electron-donating tendency from the donor orbitals and a more extensive degree of conjugation throughout the molecular system (Ghaedi, 2021). The second-order perturbation theory analysis of the Fock matrix in the NBO basis of the molecule's strong intramolecular hyper-conjugative interactions (i.e., E(2) kcal/mol) are presented in Table S1 (supplementary material).

The transition from N3[LP(1)] to S1-C9(σ∗) dominates the interactions with large second-order stabilization energy 68.90 kcal/mol, indicating strong hyperconjugation between the nitrogen lone pair and adjacent S1-C9(σ∗) anti-bond with significant electron delocalization. This delocalization significantly stabilizes the molecule and suggests that the N3 lone pair plays a major role in the electronic structure. Further, electron delocalization from O2[LP(2)] to S1-C9(σ∗) and S1[LP(2)] to O2-C9(σ∗) with the stabilization energy 43.67 kcal/mol and 17.54 kcal/mol respectively, contributes to the stability of the molecule.

Fukui functions analysis

Fukui functions serve as key descriptors for determining the regions of a molecule that exhibit the highest chemical reactivity, identifying potential sites for both electrophilic and nucleophilic attacks (Zamora et al., 2021). The Fukui function (Zamora et al., 2021) is expressed as

$$f(r) = \left[\frac{\partial \rho(\vec{r})}{\partial N}\right]_{v(r)} \qquad (13)$$

Where, N is the total number of electrons, ρ(r) is electron density and V(r) is potential due to all nuclei on an electron. To quantify the likelihood of each atom in a molecule acting as a reactive site, condensed Fukui functions are utilized. These functions assign numerical values to individual atoms, with f_k^+ and f_k^- representing the respective condensed Fukui functions (Yang et al., 2012).

$f_j^+ = [q_j(N+1) - q_j(N)]$, for nucleophilic attack (14)

$f_j^- = [q_j(N) - q_j(N-1)]$, for electrophilic attack (15)

$f_j^0 = \frac{1}{2}[q_j(N+1) - q_j(N-1)]$, for the radical attack, (16)

Here, q_j is the electronic population of atom 'j' in the (N) neutral, (N-1) cationic and (N+1) anionic state. However, for the better understanding of nucleophilicity and electrophilicity (Palego et al., 2016), a new descriptor, dual descriptor ($\Delta f(r)$) was defined as

$\Delta f(r) = [f_j^+ - f_j^-]$ (17)

When $\Delta f(r)>0$, the site is identified as electrophilic, whereas $\Delta f(r) <0$, indicates a nucleophilic site.

In the case of Cleomin, the electronic population was calculated by Natural Population Analysis (NPA) and Fukui functions were analyzed using the UCI-FUKUI_v2 tool. The computed data for the studied molecule are presented in Table 4. The calculated values (i.e., $\Delta f(r)>0$) for atoms C4, C5, C6, C8, H10, H11, H12, H13, H14, H15, H16, H17, H18, H19, and H20 indicate electrophilic regions and favor nucleophilic attack. Conversely, the calculated values (i.e., $\Delta f(r)<0$) observed for atoms S1, O2, N3, C7, and C9 suggest the nucleophilic regions and are prone to electrophilic attack. The order of nucleophilic attack susceptibility in Cleomin follows H10 > H11 > H17 > H12 > H16 > C5 > H14 > H13 > H20 > H18 > H15 > H19 > C6 > C4 > C8. In contrast, the decreasing order of sensitivity toward electrophilic attack follows S1 > N3 > O2 > C9 > C7.

Table 4. Fukui functions and Dual descriptors calculated based on the natural charges which are obtained from Natural Population Analysis (NPA) for Cleomin

Atoms	Natural Charges			Fukui Functions			Dual Descriptor
	Neutral	Cation	Anion	$f^+(r)$	$f^-(r)$	$f^0(r)$	$\Delta f(r)$
S1	-0.1705	0.5334	-0.2387	0.0682	0.7039	0.3860	-0.6357
O2	-0.5547	-0.4953	-0.5586	0.0039	0.0594	0.0316	-0.0555
N3	-0.6358	-0.5517	-0.6372	0.0014	0.0841	0.0427	-0.0828
C4	0.2625	0.2726	0.2510	0.0116	0.0100	0.0108	0.0015
C5	-0.1873	-0.1984	-0.2312	0.0439	-0.0110	0.0164	0.0329
C6	-0.3956	-0.4040	-0.4096	0.0140	-0.0085	0.0028	0.0055
C7	-0.6002	-0.6087	-0.6071	0.0069	-0.0085	0.0008	-0.0016
C8	-0.5814	-0.5862	-0.5867	0.0053	-0.0049	0.0002	0.0005
C9	0.3825	0.3643	0.3987	-0.0161	-0.0182	0.0172	-0.0021
H10	0.2023	0.2391	-0.0379	0.2403	0.0368	0.1385	0.2035
H11	0.1886	0.2207	0.0458	0.1428	0.0321	0.0875	0.1107
H12	0.2037	0.2302	0.1002	0.1035	0.0265	0.0650	0.0770
H13	0.2073	0.2131	0.1767	0.0305	0.0058	0.0182	0.0247
H14	0.2111	0.2116	0.1809	0.0302	0.0004	0.0153	0.0298
H15	0.2232	0.2385	0.1996	0.0235	0.0154	0.0194	0.0082
H16	0.2072	0.2356	0.1206	0.0867	0.0284	0.0575	0.0583
H17	0.4231	0.4426	0.3026	0.1205	0.0196	0.0700	0.1009
H18	0.1945	0.2072	0.1676	0.0270	0.0126	0.0198	0.0143
H19	0.2155	0.2088	0.2008	0.0146	-0.0067	0.0040	0.0079
H20	0.2039	0.2267	0.1624	0.0415	0.0228	0.0322	0.0186

Vibrational analysis

Figure 10 depicts the infrared spectrum of a $C_6H_{11}NOS$ in the range 0-4000 cm^{-1}. The varieties of vibrational modes result from the interaction of materials with infrared radiation (Rai et al., 2021; Khadka et al., 2023). It shows the measurement of absorption of infrared light by molecules, which causes vibrational transitions in the bonds of the molecule. The title molecule has 20 atoms and 54 (3N-6; N number of atoms) modes of vibration. All the theoretical vibrational frequencies for B3LYP/6-311++G (d, p) have been scaled down by 0.961.

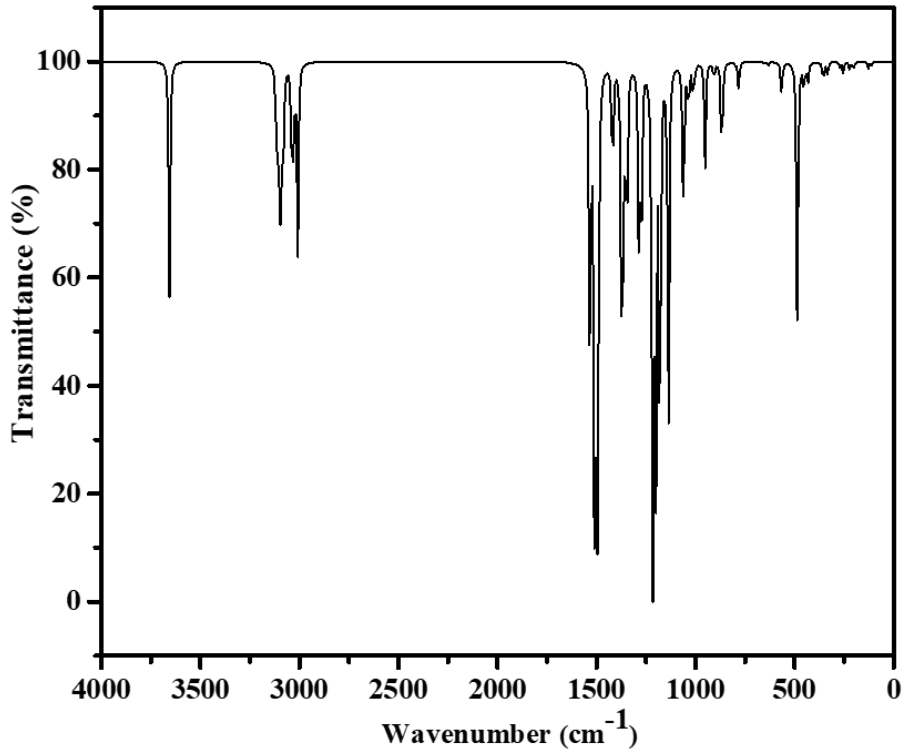

Figure 10. FT-IR curve of the Cleomin molecule

C-H vibrations

In heterocyclic molecules, the C-H stretching vibrational mode is predicted to occur in the region of 3080–3000 cm^{-1} (Stuart, 2004). Here, the observed C-H symmetric vibrations (stretching) are at 2891.03 cm^{-1}, 2910.45 cm^{-1}, 2917.18 cm^{-1}, 2922.01 cm^{-1}. The C-H antisymmetric (stretching) vibrations are observed at 2966.03 cm^{-1}, 2962.04 cm^{-1}, 2971.70 cm^{-1}, 2978.77 cm^{-1}, 2988.28 cm^{-1}, 2994.45 cm^{-1}. The C-H bending vibrations are assumed to occur < 1500 cm^{-1} (Stuart, 2004). Here, the observed C-H scissoring vibrations are 1426.22 cm^{-1}, 1432.51 cm^{-1}, 1436.18 cm^{-1}, 1445.93 cm^{-1}, 1449.82 cm^{-1}, 1451.79 cm^{-1}, 1473.76 cm^{-1}. The wagging vibrations at 1312.39 cm^{-1}, 1322.24 cm^{-1}, 1362.56 cm^{-1}, 1365.13 cm^{-1}, the twisting vibrations at 1134.71 cm^{-1}, 1224.18 cm^{-1}, 1235.26 cm^{-1}, 1294.82 cm^{-1}, and the rocking vibrations at 1029.23 cm^{-1}, 1093.16 cm^{-1} are found, respectively. This shows that the theoretical values are in good agreement with the vibrational range.

N-H vibrations (stretching)

N-H vibrations (stretching) for cyclic heterocyclic molecules appear around 3200–3500 cm^{-1} (Stuart, 2004). In Figure 10, the stretching vibration between N3 and H17 is seen at 3513.60 cm^{-1}. In this case, the N-H vibration seems to be a bit higher than the standard vibration range.

C=S stretching vibrations

Thiocarbonyl group where the C=S group is attached to elements other than nitrogen (e.g., carbon, sulfur, oxygen, chlorine), the C=S stretching vibration is generally found in the region of 1025-1225 cm^{-1} (Rao & Venkataraghavan, 1962). However, in the nitrogen-containing thiocarbonyl group, strong vibrational coupling is operative, leading to mixed vibrations and making the C=S stretching vibration not localized (Rao & Venkataraghavan, 1962). The wide range of reported C=S stretching frequencies (850 to 1570 cm^{-1}) in these compounds is primarily due to these vibrational coupling effects (Rao & Venkataraghavan, 1962). The observed vibrations for the title molecule are 872.48 cm^{-1}, 915.20 cm^{-1}, 1093.16 cm^{-1}, 1134.71 cm^{-1}, 1155.66 cm^{-1}, 1170.19 cm^{-1}, 1235.26 cm^{-1}, and 1322.24 cm^{-1} respectively.

C-N stretching vibrations

C-N stretching vibrations range between 1200-1350 cm^{-1} (Kalsi, 2007). The observed vibrations from the FT-IR curve are at 1170.19 cm^{-1}, 1224.18 cm^{-1},

1235.26 cm^{-1}, and 1294.82 cm^{-1}, and are found to lie within the theoretical range.

C-O stretching vibrations

The C-O stretching vibrations appears in the range 1000-1300 cm^{-1} (Kalsi, 2007). In this molecule, C-O vibrations are found at 1134.71 cm^{-1}, 1155.66 cm^{-1}, and 1294.82 cm^{-1}, and are within the given range.

C-C stretching vibrations

It is expected that C-C stretching vibrations appears in the range 800–1200 cm^{-1} (Socrates, 2004). From the FT-IR curve, we observed that the C-C stretching vibrations appear at 752.16 cm^{-1}, 872.48 cm^{-1}, 973.03 cm^{-1}, and 1235.26 cm^{-1}. Therefore, it can be concluded that the C-C vibrations lie within the range.

Thermodynamic analysis

Various thermodynamical quantities such as heat capacity at constant volume (C_v), heat capacity at constant pressure (C_p), total internal energy (U), enthalpy (H), entropy (S), and Gibbs free energy (G) are used to characterize both the direction and state of a chemical process. Due to the impacts of temperature on different thermodynamical variables, the measurement shows the sudden nature of a reaction and its energy profile, and it indicates whether it is endothermic or exothermic (Uprety et al., 2024). The important thermodynamic functions like total energy, zero-point energy, and rotational constant for Cleomin were calculated at room temperature 298.15K and values so obtained are presented in Table 5.

Table 5. The calculated thermodynamical parameters of Cleomin at 298.15K in the ground state at B3LYP/6-311++G (d,p) level

Parameter	Symmetry group	Total energy eV	Sp. heat (C_v) J/K/mol	Dipole moment Debye	Zero-point energy J/mol	Entropy J/K/mol	Enthalpy kJ/mol	Rotational constant GHz	Polarizability (α) a.u
B3LYP/6-311++G (d,p)	C_1	-20778.01	150.04	6.57	441153.5	401.00	466.47	2.90	105.34

The quadratic equations 18 to 20 have been obtained from the second-order polynomial fit between the dependent variable (thermodynamic quantities) and an independent variable (temperature).

$$C^0_{p,m} = 26.14279 + 0.46365T - 6.29698 \times 10^{-5}T^2 \quad (18)$$

$$H^0_m = 441.06176 + 0.02918T + 2.1630 \times 10^{-4}10^2 \quad (19)$$

$$S^0_m = 198.71953 + 0.82719T - 4.6078 \times 10^{-4}T^2 \quad (20)$$

Figure 11 shows thermodynamic quantities, i.e., $C^0_{p,m}$, H^0_m, and S^0_m are recorded with the variation of temperature between 0 K and 500 K. The correlation equations from 18 to 20 (Janani et al., 2021) illustrated in Figure 11 indicate the positive correlation of $C^0_{p,m}$, H^0_m, and S^0_m with temperature. The R^2 values for $C^0_{p,m}$, H^0_m and S^0_m are obtained as 0.99984, 1, and 0.99623, respectively. These R^2 values approximately equal to 1.0 indicate an excellent fit and show that thermodynamic parameters of the molecule are highly dependent on temperature. Therefore, the curves of $C^0_{p,m}$, H^0_m, and S^0_m increase with temperature. Besides this, the rise of $C^0_{p,m}$, H^0_m, and S^0_m with temperature also depends on the vibrational contribution. Heat capacity and entropy rise with temperature due to the gradual activation of higher-energy vibrational modes. In addition to translational and rotational degrees of freedom, this offers a denser collection of accessible microstates. These constant ground-state vibrations, which define the system's actual energetic baseline, are taken into account via zero-point energy (ZPE) corrections. Although the population of various modes can loosen unique bonds and potentially lower the activation barrier to thermal breakdown or rearrangement, this vibrational framework is still an overlooked method for assessing reaction stability at higher temperatures. As a result, the thermodynamic profile includes the structural strength and potential energy surface that regulate the compound's reactivity along with temperature.

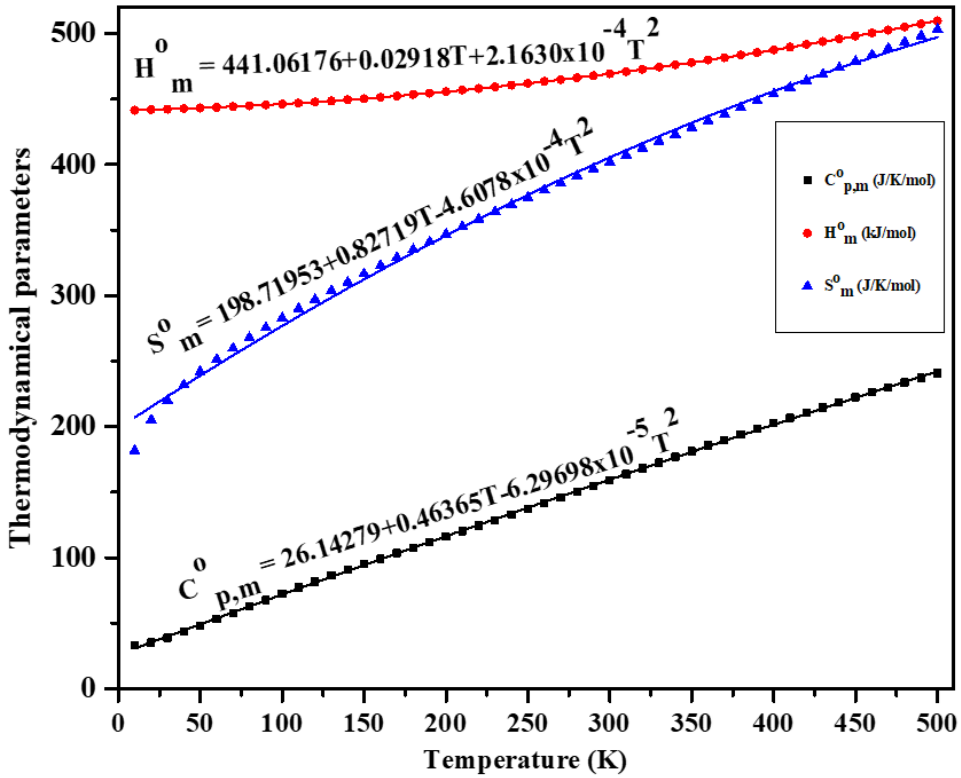

Figure 11. Correlation graph of thermodynamical parameters (i. e. $C^0_{p,m}$, H^0_m and S^0_m) with varying temperature (K)

CONCLUSION

This study employed DFT, with the B3LYP/6-311++G(d,p), WX97XD/6-311++G(d,p), and WX97XD/6-31++G(d,p) level of theory to analyze the molecular structure of Cleomin, while the B3LYP /6-311++G(d,p) basis set was further utilized to analyze its electronic, vibrational, and thermodynamic properties. Geometrical analysis revealed the longest bond (1.65 Å) at C9–S1, the largest bond angle (127.46°) at S1–C9–N3, and the highest dihedral angle (175.11°) across S1–C9–O2–C4. NCI-RDG analysis identified strong steric repulsion in the ring and ethyl group and weak H-bond interaction. ELF and LOL maps confirmed strong electron localization and bonding in the vicinity of hydrogen and sulfur atoms. The MEP mapping showed electropositive region around hydrogen bonded with nitrogen and an electronegative region near sulfur, indicating the polar centers. The HOMO and LUMO energies were determined to be -5.88 eV and -0.65 eV, respectively, yielding an energy gap of 5.23 eV, which was further proven by the DOS-derived gap value of 5.19 eV, accompanied by negligible intramolecular charge transfer (ICT). The global reactivity descriptors such as the electronegativity (χ = 2.18 eV), chemical hardness (η = 2.61 eV), chemical softness (S = 0.38 eV^{-1}), chemical potential (μ = -2.18 eV), and electrophilicity index (ω = 0.91 eV), collectively indicate that Cleomin is a chemically stable and relatively less reactive compound. Mulliken charge analysis identified S1 as an atom having highest negative charge, and H17 as an atom having highest positive charge, indicating that S1 and H17 are reactive sites for this molecule. The NBO analysis showed that the transition from N3[LP(1)] to S1-C9($\sigma*$) dominates the interactions, with a large second-order stabilization energy of 68.90 kcal/mol indicating strong hyper-conjugation between the nitrogen lone pair and adjacent S1-C9($\sigma*$) anti-bonds with significant electron delocalization. This delocalization significantly stabilizes the molecule and suggests that the N3 lone pair plays a major role in the electronic structure. Similarly, Fukui function analysis further showed that the nucleophilic attack susceptibility decreases in the order H10 > H11 > H17 > H12 > H16 > C5 > H14 > H13 > H20 > H18 > H15 > H19 > C6 > C4 > C8. In contrast, the decreasing order of sensitivity toward electrophilic attack follows S1 > N3 > O2 > C9 > C7. Theoretical vibrational wavenumbers for C-C, C-H, C-N, C-O, N-H, and C=S modes showed excellent agreement with experimentally reported FT-IR data, validating the reliability of the chosen computational methodology. Thermodynamic analysis demonstrated that, with increasing temperature, Cleomin exhibits progressive increases in heat absorption, heat capacity, and

entropy, as described by quadratic temperature dependence. Collectively, these findings provide valuable molecular-level insights into the structural, electronic, and reactive properties of Cleomin, establishing a foundation for its prospective applications in medicinal chemistry and drug design, including considerations of pharmacological activity, metabolic behavior, and toxicity profiling.

ACKNOWLEDGMENTS

The authors would like to thank Department of Physics, Patan Multiple Campus, Lalitpur, Nepal and University Grant Commission, Nepal for their support and for collaborative research [CRG-78/79-S&T-03]. We are also grateful to the St. Xavier's College, Maitighar, Kathmandu, Nepal, for software facilities.

AUTHORS CONTRIBUTION

Conceptualization: DT, KBR; Methodology: DT, KBR, ARM, BB; Validation: KBR, MPG; Investigation: DT, KBR, ARM, BB, MPG; Data Analysis: DT, KBR; Data Analysis: DT, KBR, MPG; Writing-original draft: DT; Writing-review & editing: DT, KBR, MPG

DATA AVAILABILITY STATEMENT

All data underlying the results reported in this study can be obtained from the corresponding author upon reasonable request.

FUNDING

University Grant Commission, Nepal collaborative research [CRG-78/79-S&T-03]

ORCIDs

Dipak Thapa:
https://orcid.org/0009-0006-2741-482X
Krishna Bahadur Rai:
https://orcid.org/0000-0001-8882-0385
Tulsi Ojha:
https://orcid.org/0009-0000-7507-7473
Madhav Prasad Ghimire:
https://orcid.org/0000-0003-2783-4008

CONFLICTS OF INTEREST

The authors declare that there are no conflicts of interest regarding the publication of this article.

ETHICAL STATEMENT

The authors state that it is their original work and has not been previously published or submitted for publication elsewhere.

DATA AVAILABILITY STATEMENT

The data that supports the findings of this study are available from the corresponding author upon reasonable request.

SUPPLEMENTARY INFORMATION

Table S1. Second Order Perturbation Theory Analysis of Fock Matrix in NBO Basis for Cleomin molecule using B3LYP/6-311++G(d,p) level calculation.The interactions involve donor orbitals such as σ , π , lone pair (LP), core orbital (CR) and acceptor orbitals such as $\sigma*$, $\pi*$, and Ry* (Rydberg)

REFERENCES

Alrabiah, H., Muthu, S., Al-Omary, F., Al-Tamimi, A. M., Raja, M., Muhamed, R. R., & El-Emam, A. A. R. (2017). Molecular structure, vibrational spectra, NBO, Fukui function, HOMO-LUMO analysis and molecular docking study of 6-[(2-methylphenyl) sulfanyl]-5-propylpyrimidine-2, 4 (1H, 3H)-dione. *Macedonian Journal of Chemistry and Chemical Engineering, 36*(1), 59–80.https://doi.org/10.20450/mjcce.2017.1001

Arulaabaranam, K., Muthu, S., Mani, G., & Geoffrey, A. B. (2021). Speculative assessment, molecular composition, PDOS, topology exploration (ELF, LOL, RDG), ligand-protein interactions, on 5-bromo-3-nitropyridine-2-carbonitrile. *Heliyon*, *7*(5). e07061. https://doi.org/10.1016/j.heliyon.2021.e07061

Bakheit, A. H., Al-Salahi, R., & Al-Majed, A. A. (2022). Thermodynamic and computational (DFT) study of non-covalent interaction mechanisms of charge transfer complex of linagliptin with 2, 3-dichloro-5, 6-dicyano-1, 4-benzoquinone (DDQ) and chloranilic acid (CHA). *Molecules*, *I*(19), 6320. https://doi.org/10.3390/molecules27196320

Basnet, B., Magar, A. R., Ghimire, R., Joshi, U., & Rai, K. B. (2024). First-principles calculations to investigate structural, Spectroscopic Features, Electronic and Thermodynamic Properties of Trichloroacetaldehyde. *Himalayan Journal of Science and Technology*, *8*(1), 1–9. https://doi.org/10.3126/hijost.v8i1.83091

Becke, A. D., & Edgecombe, K. E. (1990). A simple measure of electron localization in atomic and molecular systems. *The Journal of Chemical Physics*, *92*(9), 5397–5403. https://doi.org/10.1063/1.458517

Bishwokarma, N., Budha, C., Teemilsina, N. K., & Rai, K. B. (2025). Exploring vibrational spectra, electronic properties and thermal analysis of

isoguanine molecule using DFT. *Scientific World*, *18*(18), 5–14. DOI: https://doi.org/10.3126/sw.v18i18.78512

Bisong, E. A., Louis, H., Unimuke, T. O., Odey, J. O., Ubana, E. I., Edim, M. M., Tinhe, F. T., Agwupuye, J.A., & Utsu, P. M. (2020). Vibrational, electronic, spectroscopic properties, and NBO analysis of p-xylene, 3, 6-difluoro-p-xylene, 3, 6-dichloro-p-xylene and 3, 6-dibromo-pxylene: DFT study. *Heliyon*, *6*(12). https://doi.org/10.1016/j.heliyon.2020.e05783

Budha, C., & Rai, K. B. (2024). Study of the molecular structure, spectroscopic analysis, electronic structures and thermodynamic properties of niacin molecule using first-principles. *Journal of Nepal Chemical Society*, *44*(2), 1–12. https://doi.org/10.3126/jncs.v44i2.68263

Chand, S., Al-Omary, F. A., El-Emam, A. A., Shukla, V. K., Prasad, O., & Sinha, L. (2015). Study on molecular structure, spectroscopic behavior, NBO, and NLO analysis of 3-methylbezothiazole-2-thione. *Spectrochimica Acta Part A: Molecular and Biomolecular Spectroscopy*, *146*, 129–141. https://doi.org/10.1016/j.saa.2015.03.068

Chaudhary, T., Chaudhary, M. K., Jain, S., Tandon, P., & Joshi, B. D. (2023). The experimental and theoretical spectroscopic elucidation of molecular structure, electronic properties, thermal analysis, biological evaluation, and molecular docking studies of isococculidine. *Journal of Molecular Liquids*, *391*, 123212. https://doi.org/10.1016/j.molliq.2023.123212

Dennington, R., Keith, T., & Millam, J. (2009). GaussView, Version 5. Semichem Inc., Shawnee Mission, KS.

Dhanalakshmi, E., Rajesh, P., Arunkumar, K., Gnanasambandan, T., Issaoui, N., Sudha, K., & Raja, M. (2023). Synthesis, GCMS, spectroscopic, electronic properties, chemical reactivity, RDG, topology and biological assessment of 1-(3, 6, 6-trimethyl-1, 6, 7, 7a-tetrahydrocyclopenta [c] pyran-1-yl) ethanone. *Chemical Physics Impact*, *7*, 100385. https://doi.org/10.1016/j.chphi.2023.100385

Elanthiraiyan, M., Jayasudha, B., & Arivazhagan, M. (2015). Molecular structure, vibrational spectroscopy, NBO and HOMO, LUMO studies of o-methoxybenzonitrile. Spectrochimica *Acta Part A: Molecular and Biomolecular Spectroscopy*, *134*, 543–552. https://doi.org/10.1016/j.saa.2014.04.103

Frisch, M. J., Trucks, G. W., Schlegel, H. B., Scuseria, G. E., Robb, M. A., Cheeseman, J. R., Scalmani, G., Barone, V., Mennucci, B., Petersson, G. A., Nakatsuji, H., Caricato, M., Li, X., Hratchian, H. P., Izmaylov, A. F., Bloino, J., Zheng, G., Sonnenberg, J. L., Hada, M., Ehara, M., … & Fox, D. J. (2009). Gaussian 09 (Revision D.01). Gaussian, Inc., Wallingford CT.

Ghaedi, M. Ed. (2021). Photocatalysis: fundamental processes and applications (Vol. 32). Academic Press. https://doi.org/10.1016/c2018-0-02772-3

Ignatov, S. K. (2004). Moltran v. 2.5-Program for molecular visualization and thermodynamic calculations. University of Nizhny Novgorod.

Jacobsen, H. (2008). Localized-orbital locator (LOL) profiles of chemical bonding Canadian Journal of Chemistry, *86*(7), 695–702. https://doi.org/10.1139/v08-052

Janani, S., Rajagopal, H., Muthu, S., Aayisha, S., & Raja, M. (2021). Molecular structure, spectroscopic (FT-IR, FT-Raman, NMR), HOMO-LUMO, chemical reactivity, AIM, ELF, LOL and Molecular docking studies on 1-Benzyl-4-(N-Boc-amino) piperidine. *Journal of Molecular Structure*, *1230*, 129657. https://doi.org/10.1016/j.molstruc.2020.129657

Johnson, E. R., Keinan, S., Mori-Sánchez, P., Contreras-García, J., Cohen, A. J., & Yang, W. (2010). Revealing noncovalent interactions. *Journal of the American Chemical Society*, *132*(18), 6498–6506. https://doi.org/10.1021/ja100936

Kalsi, P. S. (2007). Spectroscopy of organic compounds. New Delhi, India; New age international.

Kederiene, V., Rousseau, J., Schuler, M., Sackus, A., & Tatibouët, A. (2022). Copper-catalyzed S-arylation of furanose-fused oxazolidine-2-thiones. *Molecules*, *27*(17), 5597. https://doi.org/10.3390/molecules27175597

Khadka, I. B., Rai, K. B., Alsardia, M. M., Haq, B. U., & Kim, S. H. (2023). Raman investigation of substrate-induced strain in epitaxially grown graphene on low/high miscut angled silicon carbide and its application perspectives. *Optical Materials*, *140*, 113836. https://doi.org/10.1016/j.optmat.2023.113836

Khalili, F., Vafaee, M., Cho, D., & Shokri, B. (2021). Charge migration in caffeine: A real-time time-dependent density functional theory study. *International Journal of Quantum Chemistry*, *121*(19), e26754. https://doi.org/10.1002/qua.26754

Kjaer, A. (1963). Isothiocyanates of natural derivation. *Pure and Applied Chemistry*, *7*(2–3),

229–246. https://doi.org/10.1351/pac196307020229

Kumar, S., & Choudhary, M. (2023). Design and molecular docking studies of {N1-[2-(amino) ethyl] ethane-1, 2-diamine}-[tris (oxido)]-molybdenum (VI) complex as a potential antivirus drug: from synthesis to structure. *Journal of Coordination Chemistry, 76*(2), 322–344. https://doi.org/10.1080/00958972.2023.2173589

Lakshminarayanan, S., Jeyasingh, V., Murugesan, K., Selvapalam, N., & Dass, G. (2021). Molecular electrostatic potential (MEP) surface analysis of chemo sensors: An extra supporting hand for strength, selectivity & non-traditional interactions. *Journal of Photochemistry and Photobiology, 6*, 100022. https://doi.org/10.1016/j.jpap.2021.100022

Lu, T., & Chen, F. (2012). Multiwfn: A multifunctional wavefunction analyzer. *Journal of Computational Chemistry, 33*(5), 580–592. https://doi.org/10.1002/jcc.22885

Mathammal, R., Sangeetha, K., Sangeetha, M., Mekala, R., & Gadheeja, S. (2016). Molecular structure, vibrational, UV, NMR, HOMO-LUMO, MEP, NLO, NBO analysis of 3, 5 di tert butyl 4 hydroxy benzoic acid. *Journal of Molecular Structure, 1120*, 1–14. https://doi.org/10.1016/j.molstruc.2016.05.008

Miar, M., Shiroudi, A., Pourshamsian, K., Oliaey, A. R., & Hatamjafari, F. (2021). Theoretical investigations on the HOMO–LUMO gap and global reactivity descriptor studies, natural bond orbital, and nucleus-independent chemical shifts analyses of 3-phenylbenzo [d] thiazole-2 (3 H)-imine and its para-substituted derivatives: Solvent and substituent effects. *Journal of Chemical Research, 45*(1–2), 147–158.

O'Boyle, N. M., Tenderholt A. L., & Langner K. M. (2008) Cclib: A library for package-independent computational chemistry algorithms. *Journal of Computational Chemistry; 29(5)*: 839–845. https://doi.org/10.1002/jcc.20823

Oguakwa, J. U., Patamia, M., Galeffi, C., Messana, I., & Nicoletti, M. (1981). Isolation of Cleomin from roots of *Ritchiea longipedicillata*. *Planta medica, 41*(04), 410–412. https://doi.org/10.1055/s-2007-971739

Ojha, T., Shrestha, P. M., Gupta, S.P., & Rai, K. B. (2025). Quantum chemical insights into the electronic, vibrational and thermodynamic properties of chloro-substituted anisole. *Al-Nahrain Journal Science, 28* (4), 146–164. https://doi.org/10.22401/anjs.28.4.12

Opretzka, L. C. F., Viana, M. D. M., de Lima, A. A., de Souza, T. A., Scotti, M. T., Tavares, J. F., da Silva, M. S., Soaves, M. B. P., & Villarreal, C. F. (2023). Cleomin exerts acute antinociceptive effects in mice via GABAB and muscarinic receptors. *Pharmaceuticals, 16*(11), 1547. https://doi.org/10.3390/ph16111547

Palego, L., Betti, L., Rossi, A., & Giannaccini, G. (2016). Tryptophan biochemistry: structural, nutritional, metabolic, and medical aspects in humans. *Journal of amino acids*, (1), 8952520. https://doi.org/10.1155/2016/8952520

Pîrnau, A., Chiş, V., Oniga, O., Leopold, N., Szabo, L., Baias, M., & Cozar, O. (2008). Vibrational and DFT study of 5-(3-pyridyl-methylidene)-thiazolidine-2-thione-4-one. *Vibrational spectroscopy, 48*(2), 289–296. https://doi.org/10.1016/j.vibspec.2008.01.012

Rai, K. B., Khadka, I. B., Koirala, A. R., & Ray, S. K. (2021). Insight of cleaning, doping and defective effects on the graphene surface by using methanol. *Advances in Materials Research, 10*(4), 283–292. 10.12989/amr.2021.10.4.283

Rajalakshmi, K., & Vetrivel, M. (2020). NBO and topology (MESP, ELF, LOL) analysis of 2-hydroxypropanamide. *International Journal of Advance Scientific Research and Engineering Trends, 5*(4), 50–58.

Ram, V. J., Sethi, A., Nath, M., & Pratap, R. (2019). Five-membered heterocycles. *The Chemistry of Heterocycles*, 149–478. https://doi.org/10.1016/b978-0-08-101033-4.00005-x

Rao, C. N. R., & Venkataraghavan, R. (1962). The C= S stretching frequency and the "-NC= S bands" in the infrared. *Spectrochimica Acta, 18*(4), 541–547. https://doi.org/10.1016/s0371-1951(62)80164-7

Roux, M. V., Temprado, M., Jiménez, P., Foces-Foces, C., Notario, R., Parameswar, A. R., Demchenko, A. V., Chickos, J. S., Deakyne, C. A., Ludden, A. K., & Liebman, J. F. (2009). Experimental and theoretical study of the structures and enthalpies of formation of the synthetic reagents 1, 3-Thiazolidine-2-thione and 1, 3-Oxazolidine-2-thione. *The Journal of Physical Chemistry A, 113*(40), 10772–10778. https://doi.org/10.1021/jp9034216

Savin, A. (2005). The electron localization function (ELF) and its relatives: interpretations and difficulties. *Journal of Molecular Structure: THEOCHEM, 727*(1-3), 127–131. https://doi.org/10.1016/j.theochem.2005.02.034

Savin, A., Nesper, R., Wengert, S., & Fässler, T. F. (1997). ELF: The electron localization function. Angewandte Chemie International Edition in English. 36(17), 1808–1832. https://doi.org/10.1002/anie.199718081

Schmider, H. L., & Becke, A. D. (2000). Chemical content of the kinetic energy density. *Journal of Molecular Structure: THEOCHEM*, *527*(1–3), 51–61. https://doi.org/10.1016/s0166-1280(00)00477-2

Schmider, H. L., & Becke, A. D. (2002). Two functions of the density matrix and their relation to the chemical bond. *The Journal of Chemical Physics*, *116*(8), 3184–3193. https://doi.org/10.1063/1.1431271

Shilpa, D., Sadasivam, K., & Thirumoorthy, M. (2023). Topology analysis of six phytochemicals through ELF and LOL basins - A DFT study. *Indian Journal of Chemistry (IJC)*, *62*(11), 1171–1177. https://doi.org/10.56042/ijc.v62i11.2900

Socrates, G. (2004). Infrared and Raman characteristic group frequencies: tables and charts. John Wiley & Sons. https://doi.org/10.1002/jrs.1238

Stuart, B. H. (2004). Infrared spectroscopy: fundamentals and applications. John Wiley & Sons. https://doi.org/10.1002/0470011149

Sworakowski, J. (2018). How accurate are energies of HOMO and LUMO levels in small-molecule organic semiconductors determined from cyclic voltammetry or optical spectroscopy? *Synthetic Metals*, *235*, 125–130. https://doi.org/10.1016/j.synthmet.2017.11.013

Tahenti, M., Issaoui, N., Roisnel, T., & Marouani, H. (2022). Synthesis, characterization, and computational survey of a novel material template o-xylylenediamine. *Journal of the Iranian Chemical Society*, *19*(4), 1499–1514. https://doi.org/10.1007/s13738-021-02392-9

Uprety, R., Ghimire, R., Magar, P. G., Rokka, D., Khadka, I. B., Neupane, R., & Rai, K. B. (2024). Study of the molecular structure, electronic structure, spectroscopic analysis and thermodynamic properties of dibenzofuran using first principles. *Journal of Nepal Physical Society*, *10*(2), 8–18. https://doi.org/10.3126/jnphyssoc.v10i2.79470

William, H. (1996). VMD-visual molecular dynamics. *Journal of Molecular Graphics*, *14*, 33–38. https://doi.org/10.1016/0263-7855(96)00018-5

Yang, W., Cohen, A. J., De Proft, F., & Geerlings, P. (2012). Analytical evaluation of Fukui functions and real-space linear response function. *The Journal of Chemical Physics*, *136*(14). https://doi.org/10.1063/1.3701562

Zamora, P. P., Bieger, K., Cuchillo, A., Tello, A., & Muena, J. P. (2021). Theoretical determination of a reaction intermediate: Fukui function analysis, dual reactivity descriptor and activation energy. *Journal of Molecular Structure*, *1227*, 129369. https://doi.org/10.1016/j.molstruc.2020.129369